nature communications

Article

https://doi.org/10.1038/s41467-024-52199-4

Superoxide radical derived metal-free spiro-OMeTAD for highly stable perovskite solar cells

Received: 3 March 2024

Accepted: 28 August 2024

Published online: 10 September 2024

Check for updates

Linfeng Ye[1,2,6], Jiahao Wu[1,2,6], Sergio Catalán-Gómez[3,6], Li Yuan[1,2], Riming Sun[1,2], Ruihao Chen[1,2], Zhe Liu[1,2], Jose María Ulloa[3], Adrian Hierro[3], Pengfei Guo[1,2,4] ✉, Yuanyuan Zhou[5] & Hongqiang Wang[1,2] ✉

Lithium salt-doped spiro-OMeTAD is widely used as a hole-transport layer (HTL) for high-efficiency n-i-p perovskite solar cells (PSCs), but unfortunately facing awkward instability for commercialization arising from the intrinsic Li^+ migration and hygroscopicity. We herein demonstrate a superoxide radicals ($•O_2^-$) derived HTL of metal-free spiro-OMeTAD with remarkable capability of avoiding the conventional tedious oxidation treatment in air for highly stable PSCs. Present work explores the employing of variant-valence $Eu(TFSI)_2$ salts that could generate $•O_2^-$ for facile and adequate pre-oxidation of spiro-OMeTAD, resulting in the HTL with dramatically increased conductivity and work function. Comparing to devices adopting HTL with LiTFSI doping, the $•O_2^-$-derived spiro-OMeTAD increases the PSCs efficiency up to 25.45% and 20.76% for 0.05 cm^2 active area and 6 × 6 cm^2 module, respectively. State-of-art PSCs employing such metal-free HTLs are also demonstrated to show much-improved environmental stability even under harsh conditions, e.g., maintaining over 90% of their initial efficiency after 1000 h of operation at the maximum power point and after 80 light-thermal cycles under simulated low earth orbit conditions, respectively, indicating the potentials of developing metal-free spiro-OMeTAD for low-cost and shortened processing of perovskite photovoltaics.

Regular planar halide perovskite solar cells (PSCs), which consist of an active perovskite layer sandwiched between electron- and hole-transporting layers (ETLs and HTLs), have attracted extensive interest owing to their outstanding photovoltaic performance and easy fabrication process. Currently, the state-of-the-art PSCs with power conversion efficiencies (PCE) exceeding 25% rely on the benchmark HTL of 2,2′,7,7′-tetrakis[N, N-di(4-methoxyphenyl)amino]−9, 9-spirobifluorene (spiro-OMeTAD, Fig. 1a)[1–3], in which lithium bis(trifluoromethanesulfonyl)imide (LiTFSI) is typically used as a p-type dopant to enhance the hole extraction and conductivity of spiro-OMeTAD according to the subsequent reactions[4–8]: (i) spiro-OMeTAD + O_2 ↔ spiro-OMeTAD$^{•+}O_2^{•-}$; and (ii) spiro-OMeTAD$^{•+}O_2^{•-}$ + LiTFSI → spiro-OMeTAD$^{•+}TFSI^-$ + Li_xO_y. However, such a formulation typically requires an air-oxidization process for approximately 24 hours for the cationization of spiro-OMeTAD (Fig. 1b). This is time-intensive and highly dependent on ambient conditions, thereby

[1]State Key Laboratory of Solidification Processing, Center for Nano Energy Materials, School of Materials Science and Engineering, Northwestern Polytechnical University, Xi'an, China. [2]Shaanxi Joint Laboratory of Graphene (NPU), Xi'an, China. [3]ISOM, Universidad Politécnica de Madrid, Madrid, Spain. [4]Research & Development Institute of Northwestern Polytechnical University in Shenzhen, Shenzhen, China. [5]Department of Chemical and Biological Engineering, The Hong Kong University of Science and Technology, Clear Water Bay, Hong Kong SAR, China. [6]These authors contributed equally: Linfeng Ye, Jiahao Wu, Sergio Catalán-Gómez. ✉e-mail: guopengfei@nwpu.edu.cn; hongqiang.wang@nwpu.edu.cn

https://doi.org/10.1038/s41467-024-52199-4

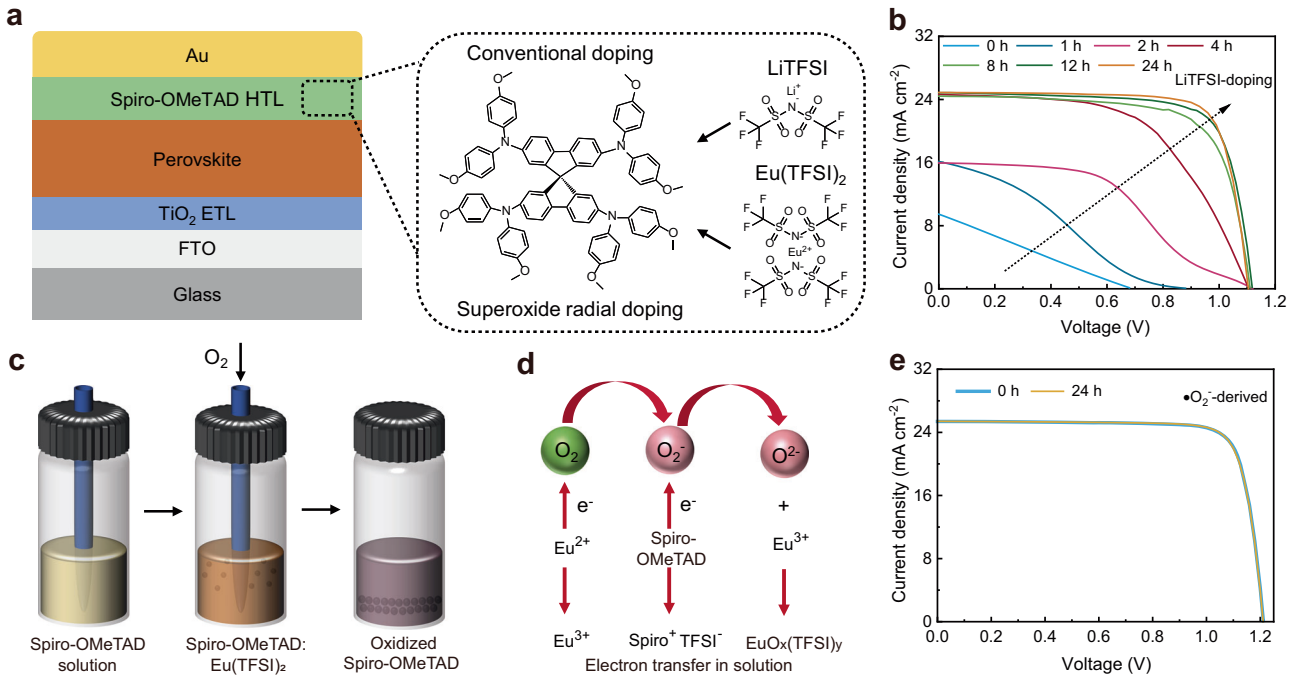

Fig. 1 | Comparison in LiTFSI-doped and $\bullet O_2^-$-derived spiro-OMeTAD HTLs. **a** Schematic illustration of a n-i-p PSC with spiro-OMeTAD HTLs doped by LiTFSI or $Eu(TFSI)_2$. **b** *J-V* curves of the LiTFSI-doped PSCs under different oxidation time. **c**, **d** Schematic illustrations of the pre-oxidation and $\bullet O_2^-$-doping process by the addition of $Eu(TFSI)_2$ in the spiro-OMeTAD solution. **e** *J-V* curves of the $\bullet O_2^-$-derived PSCs under different time. Source data are provided as a Source Data file.

hindering the commercialization of PSCs[9,10]. The inadequate doping efficacy of this post-treatment process may lead to the retention of unreacted reactants and/or detrimental by-products in the doped spiro-OMeTAD layer, thereby negatively affecting the device efficiency[10–13]. Furthermore, a significant challenge that restricts their practical application is the trade-off between high efficiency and stability. This is primarily attributable to the rapid diffusion of lithium ions along with the hydrophilicity and the lower glass transition temperature of the LiTFSI-doped spiro-OMeTAD. This ultimately contributes to the environmental instability of the PSCs and is further aggravated by external stimuli such as heat, light, and moisture[14–18]. Therefore, it is highly desirable to find a post-oxidation-free and Li-free doping strategy that enhances the selectivity for holes in the spiro-OMeTAD HTL while maintaining the balance between high efficiency and high stability in PSCs.

Tremendous efforts have been dedicated to optimizing the spiro-OMeTAD HTL for synchronously enhanced PCE and stability of PSCs. Considering that the actual doping process of the spiro-OMeTAD HTL is to attain a TFSI-stabilized radical cation (spiro-$OMeTAD^{+}TFSI^{-}$) in accordance with the above formulas, the entire process is highly dependent on the O_2 ingress, diffusion, and oxidizing ability, while the large anion $TFSI^-$ in LiTFSI merely serves as a charge balancer for the oxidized spiro-$OMeTAD^+$. Therefore, the vulnerable Li is redundant and can be removed from dopants. In order to minimize the negative effects of Li, less hygroscopic dopants such as metallic salts[19–21], dicationic salts of spiro-OMeTAD[22,23], and protic ionic liquids[24] have been incorporated as substitutes for the oxidant LiTFSI. For instance, Seo et al. used spiro-OMeTAD HTL with substantial improvements in both the photovoltaic performance and long-term moisture stability by substituting conventional LiTFSI with large-sized $Zn(TFSI)_2$[22]. Utilizing molecular additives to anchor the migrated Li ions in order to preserve the structural integrity of the spiro-OMeTAD HTL under humidity, heat, and light stress is an alternative method[2,5,25]. Although these strategies may unquestionably improve the stability of the device, they still require an air-exposure process. To obtain post-oxidation-free PSC devices, a CO_2/O_2-bubbling doping method was recently employed to pre-oxidize the spiro-OMeTAD solution under ultraviolet light, realizing highly efficient and stable PSCs without any post-treatments[4]. More recently, the pre-synthesized spiro-$OMeTAD_2^{\bullet+}(TFSI^-)_2$ radical accompanied by the doping modulation of ionic salts has been found to be directly involved in the spiro-OMeTAD HTL of PSCs without the oxidation process. This has resulted in delivering PCEs of > 25% and much-improved device stability under harsh conditions[1]. Inspired by the ion-modulated radical doping, it is well indicated that the doping efficiency of spiro-OMeTAD HTLs and subsequent device performance of PSCs are mainly determined by the content and distribution of spiro-$OMeTAD^{\bullet+}$ radicals. However, technological hurdles remain not only in the synthesis of these pre-synthesized radicals but also in their subsequent doping modulation within HTLs. Therefore, the investigation of efficient new dopants and/or doping methods still remains an ongoing pursuit for highly stable spiro-OMeTAD-based PSCs.

Herein, we developed a rapid and Li-free doping strategy for spiro-OMeTAD that avoids post-oxidation by constructing $\bullet O_2^-$ in the spiro-OMeTAD solution. The $\bullet O_2^-$ can be facilely formed in the spiro-OMeTAD solution in air with the addition of variant-valence $Eu(TFSI)_2$ salts obtained from the chemical reactions between Eu metal and HTFSI (Fig. 1c). During this process, O_2 obtains an electron from the Eu^{2+}-Eu^{3+} redox shuttle and rapidly produces the $\bullet O_2^-$, resulting in the subsequent oxidation of spiro-OMeTAD and its p-type doping (Fig. 1d). In stark contrast to conventional LiTFSI doping with air exposure, $\bullet O_2^-$-derived spiro-OMeTAD HTLs can instantly obtain high conductivity and ideal work function without requiring post-treatments, delivering their PSCs with PCEs over 25% (Fig. 1e). Furthermore, the long-term stability of the PSCs based on the $\bullet O_2^-$-derived spiro-OMeTAD HTLs is significantly enhanced due to the increased resistance toward moisture and ion migration, in addition to the lack of Li^+ and air exposure. After 5000 hours of air storage at a relative humidity of 70% without encapsulation, the resultant devices can retain 80% of their initial efficiency. Also, they maintain over 90% of their initial efficiency after 1000 hours under maximum power point operating conditions, or under thermal stress of 85 °C. In addition, $\bullet O_2^-$-derived devices exhibit remarkable light-thermal-cycling stability under simulated low earth

https://doi.org/10.1038/s41467-024-52199-4

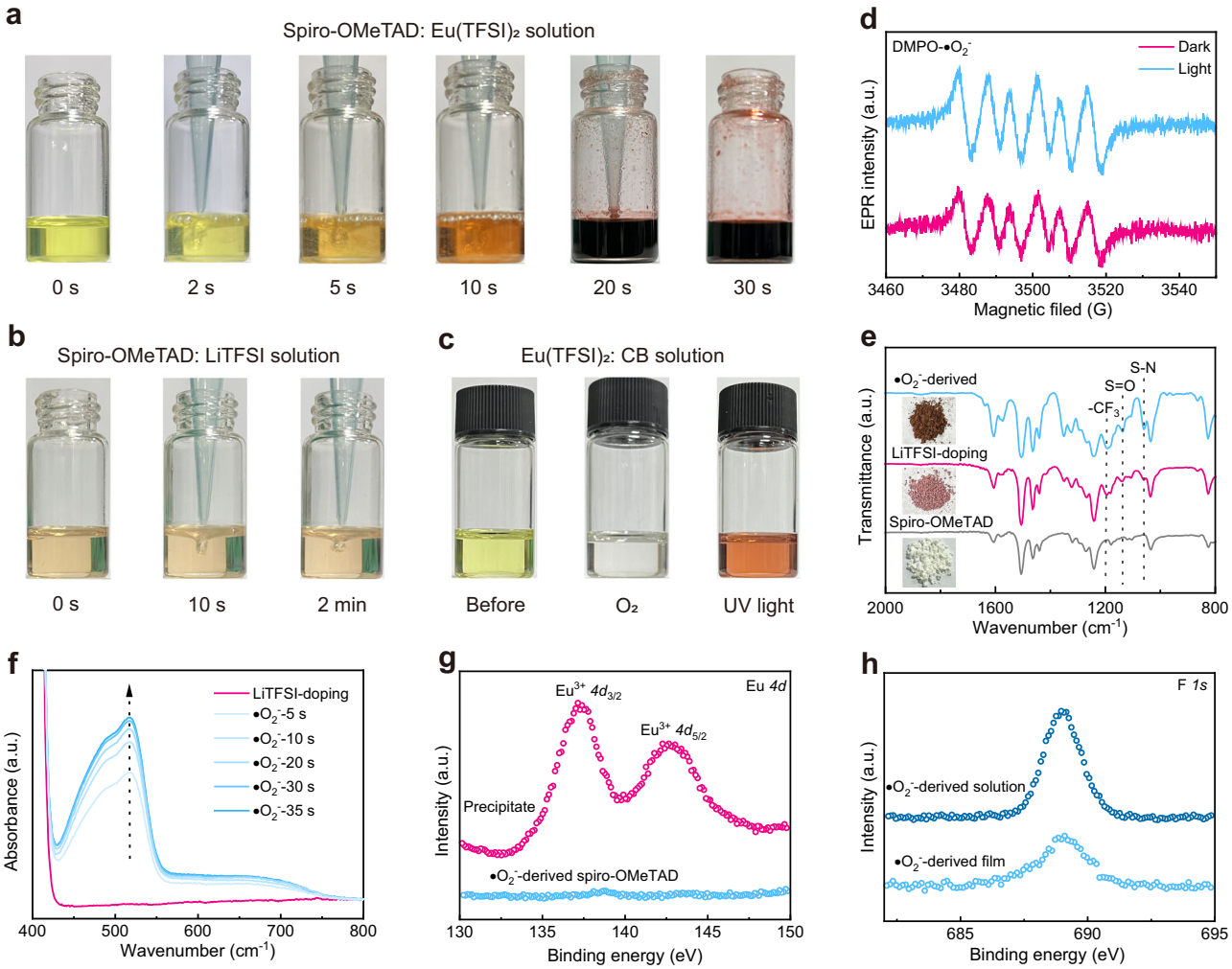

Fig. 2 | O_2^- doping mechanism. The color evolution of different solutions bubbled with O_2 under different time: **a** spiro-OMeTAD:Eu(TFSI)$_2$, **b** spiro-OMeTAD:LiTFSI, and **c** EuTFSI$_2$:CB. **d** EPR spectra of the EuTFSI$_2$:CB solution bubbled with O_2 for 10 s and tested after 5 min (5,5-dimethyl-1-pyrroline-N-oxide, DMPO). **e** FTIR spectra of the raw, LiTFSI-doped and $•O_2^-$-derived spiro-OMeTAD powder. The insets show the optical images of three powers. **f** UV-vis spectra of the $•O_2^-$ derived spiro-OMeTAD solution under different time. **g** High-resolution XPS spectra of Eu 4d for the $•O_2^-$-derived spiro-OMeTAD film and the residual precipitate. **h** High-resolution XPS spectra of F 1 s for the $•O_2^-$-derived spiro-OMeTAD solution and film. Source data are provided as a Source Data file.

orbit (LEO) conditions. In PSCs with post-oxidation-free or Li-free spiro-OMeTAD HTLs, the present $•O_2^-$-deriving work ranks among the highest in terms of both efficiency and stability (Supplementary Table 1).

Results and discussion

Superoxide radicals doping mechanism

The $•O_2^-$ deriving method is first demonstrated by bubbling the spiro-OMeTAD:Eu(TFSI)$_2$ solution with O_2 (Fig. 2a and Supplementary Movie 1), where the Eu(TFSI)$_2$ salts were facilely synthesized by chemical reactions between Eu metal and HTFSI in acetonitrile (see "Methods" section). By adding the Eu(TFSI)$_2$ with an optimal concentration of 40 mol% into the as-prepared spiro-OMeTAD solution, it can be seen that the color of the spiro-OMeTAD:Eu(TFSI)$_2$ solution rapidly changes from light yellow to dark red after 30 seconds of bubbling with O_2, indicating that the spiro-OMeTAD in solution is oxidized to form the spiro-OMeTAD$^+$[1,10]. However, in the conventional spiro-OMeTAD:LiTFSI solution, there is not much change in color when bubbled with O_2 for even 2 minutes (Fig. 2b), which is consistent with findings from previous reports[4]. Furthermore, after adding Eu(TFSI)$_2$, the spiro-OMeTAD solution can be directly oxidized in air within 30 seconds (Supplementary Fig. 1 and Supplementary Movie 2 and Supplementary Movie 3), indicating the presence of a robust oxidation medium in the spiro-OMeTAD solution.

A comparative analysis was conducted to determine the reason behind the different oxidation patterns observed in spiro-OMeTAD solutions doped with LiTFSI and Eu(TFSI)$_2$. To accomplish this, an additional solution consisting of Eu(TFSI)$_2$: chlorobenzene (CB) was prepared without spiro-OMeTAD (Fig. 2c). Strikingly, the color of the Eu(TFSI)$_2$:CB solution was changed instantly from light yellow to colorless when bubbling with O_2, indicating the transformation of Eu^{2+} to Eu^{3+}, as evidenced by the existing red phosphorescence after being irradiated by ultraviolet light[26]. The lost electron from the Eu^{2+}-Eu^{3+} redox shuttle would thus be recovered by O_2, contributing rapidly to the generation of the $•O_2^-$, which is confirmed by the electron paramagnetic resonance (EPR, Fig. 2d). The EPR recorded at room temperature in both dark and light conditions shows 6 peaks for the O_2-bubbled Eu(TFSI)$_2$:CB solution, demonstrating the generation of $•O_2^-$ in solution[27]. Furthermore, we conducted the EPR spectra on the O_2-bubbled spiro-OMeTAD:Eu(TFSI)$_2$ solution to specifically detect the signal of $•O_2^-$ in solutions with spiro-OMeTAD (Supplementary Note 1). After bubbling with O_2 for 10 s, we immediately detected the signal of $•O_2^-$ and found the presence of $•O_2^-$ in this solution based on the observation of its six peaks

(Supplementary Fig. 2a). The resultant $\bullet O_2^-$ will instantly oxidize the spiro-OMeTAD to a TFSI-stabilized spiro-OMeTAD$^+$ radical cation along with the Eu^{3+} reaction products, as evidenced by the color evolution of their solutions (Fig. 2a) and EPR spectra after sufficient oxidation (Supplementary Fig. 2b). These results significantly demonstrate that $\bullet O_2^-$ shows an improved reaction rate compared with O_2 when involved in the in situ oxidation of spiro-OMeTAD in solution (Supplementary Note 2). After filtering and drying, a dark brown and oxidized spiro-OMeTAD powder was consequently synthesized by the $\bullet O_2^-$-derived strategy, as illustrated in the insets of Fig. 2e. Therefore, the step-by-step reaction of the oxidation of spiro-OMeTAD in solution can be described as follows (Supplementary Fig. 3 and Supplementary Note 3):

$$Eu^{2+} + O_2 \rightarrow Eu^{3+} + \bullet O_2^- \quad (1)$$

$$\text{spiro-OMeTAD} + \bullet O_2^- \rightarrow \text{spiro-OMeTAD}^+ + O^{2-} \quad (2)$$

$$\text{spiro-OMeTA}^+ + TFSI^- \rightarrow \text{spiro-OMeTAD}^+ - TFSI^- \quad (3)$$

The overall reaction can be follows:

$$\text{spiro-OMeTA}^+ O_2 + Eu(TFSI)_2 \rightarrow \text{spiro-OMeTAD}^+ - TFSI^- + EuO_xTFSI_{(3-2x)} \quad (4)$$

In order to determine whether the $\bullet O_2^-$ is involved in an in situ oxidation of spiro-OMeTAD in solution, Fourier-transform infrared spectroscopy (FTIR) and ultraviolet-visible (UV-vis) absorption spectroscopy were used to check the generation of spiro-OMeTAD$^+$ radical cations, which is known to arise in oxidized spiro-OMeTAD reported in previous works[5,22]. Figure 2e shows the FTIR spectra of the pristine, LiTFSI doped (after 12 h of air exposure) and $\bullet O_2^-$-derived spiro-OMeTAD. It is clearly evident that there are emerging absorption peaks at ~1059, ~1137 and ~1195 cm^{-1} corresponding to S-N, S = O, and CF_3 bonds after the doping of spiro-OMeTAD, respectively, in which the peak intensity for the $\bullet O_2^-$-derived spiro-OMeTAD is higher than those doped by conventional LiTFSI, elucidating the strong doping ability of the $\bullet O_2^-$. As shown in Fig. 2f and Supplementary Fig. 4, the spiro-OMeTAD:$Eu(TFSI)_2$ solution bubbled with O_2 exhibits a gradually increased polaron absorption peak centered at about 521 nm with the increasing bubbling time or concentration of $Eu(TFSI)_2$. In contrast, there are no peaks emerging in the UV-vis spectra for the conventional spiro-OMeTAD:LiTFSI solution with or without O_2 bubbling. The formation of polaron peaks for the spiro-OMeTAD$^+$ can therefore be easily distinguished from ground-state spiro-OMeTAD, and serves as a pre-oxidation signal for the spiro-OMeTAD solution[4].

After the pre-oxidation of spiro-OMeTAD solution, there are two reaction products produced in the solution: oxidized spiro-OMeTAD and Eu^{3+} precipitate. The oxidized spiro-OMeTAD can be re-dissolved in the solution, whereas the insoluble precipitate can be filtered and its composition can be determined through X-ray photoelectron spectroscopy (XPS). Figure 2g and 2h show the high-resolution XPS spectra of Eu *4d* and F *1s* for the oxidized spiro-OMeTAD and derived precipitate, respectively. Two prominent peaks are located in the precipitate at 137.2 and 142.7 eV, which correspond to the Eu $4d_{3/2}$ and Eu $4d_{5/2}$, respectively. These peaks indicate the generation of trivalent Eu ions. The peak located at 688.9 eV in Fig. 2h, which corresponds to the F *1s*, signifies the existence of the $TFSI^-$ anion in the precipitate, as well as the existence of $TFSI^-$ and its coordinate spiro-OMeTAD$^+$ in the oxidized spiro-OMeTAD. Therefore, the existence form of this precipitate may be $EuO_x(TFSI)_{(3-2x)}$. Such precipitate generated in solution can be completely removed by filtration, as evidenced by the absence of Eu *4d* signals in the oxidized spiro-OMeTAD (Fig. 2g).

Properties of superoxide radicals derived spiro-OMeTAD

Figure 3a shows the differential scanning calorimetry (DSC) thermograms of the spiro-OMeTAD materials based on different doping. It can be clearly seen that the glass transition temperature (T_g) increases up to 130 °C for the $\bullet O_2^-$-derived spiro-OMeTAD, which is nearly 30 °C higher than that of LiTFSI-doping. The significant rise in T_g observed in the spiro-OMeTAD is beneficial to the thermal stability of the resultant PSC device. Then, different spiro-OMeTAD HTLs deposited onto glass and perovskite substrates were prepared to evaluate their film quality (Supplementary Fig. 5). Similarly, both films present uniform and compact surface morphology regardless of the substrates before aging in air. The pristine morphology of the $\bullet O_2^-$-derived film was observed to persist even after 24 hours of exposure to air, which is the typical oxidization time for LiTFSI-doped spiro-OMeTAD. However, many byproducts and/or voids in the LiTFSI-doped film are clearly observed. This is probably attributed to the migration and diffusion of residual Li within the spiro-OMeTAD layer[18], as well as its sensitivity to humidity in air[25].

The conductivity of different HTLs was further investigated by constructing the hole-only devices with the structure of ITO/PEDOT:PSS/doped-spiro-OMeTAD/Au. The effects of the $\bullet O_2^-$ on the HTL conductivity exhibit two distinct stages as a function of the increasing amount of $Eu(TFSI)_2$ dopants. Strikingly, there is initially an extremely high doping efficiency with a small doping ratio of $\bullet O_2^-$ ($Eu(TFSI)_2$ of 5 mol%, Fig. 3b), which could increase the conductivity of the HTL by almost three-fold better than that of the LiTFSI-doped HTL after 24 hours of oxidization, indicating efficient generation of hole polaron by the $\bullet O_2^-$-doping. With regard to higher $\bullet O_2^-$ concentrations, the current densities of corresponding devices show a linear dependence over the entire voltage range from −3 V to 3 V, indicating a higher conductivity in spiro-OMeTAD HTLs[1,28]. This increase could be attributed to the filling of deep trap states by the $\bullet O_2^-$-generated charge carriers, which in turn favors higher hole concentration and mobility (Supplementary Fig. 6 and Supplementary Note 4)[1,2,29]. It should be noted that the conductivity of HTLs would reach peak at the concentration of $\bullet O_2^-$ up to 40 mol% owing to a doping saturation phenomenon (Supplementary Note 5)[1]. Figure 3c shows the high-resolution liquid nuclear magnetic resonance (NMR), where the undoped spiro-OMeTAD exhibits peaks of 2.3, 3.8, 6.7–6.9, 7.2 and 7.3–7.4 corresponding to the aromatic protons in ^1H NMR signals (Supplementary Fig. 7). These peaks diminish significantly following $\bullet O_2^-$-doping, demonstrating that the effective electron exchange takes place between spiro-OMeTAD and spiro-OMeTAD$^+TFSI^-$ in the presence of the $TFSI^-$ stabilizer originating from $Eu(TFSI)_2$, which is consistent with previous reports[1,2].

In addition to conductivity, the charge transfer at the perovskite/spiro-OMeTAD interface is critical to PSCs performance. The steady-state and time-resolved photoluminescence (PL) spectra of different HTLs deposited on perovskite films were further conducted to investigate the interfacial loss. As shown in Fig. 3d, there is a significant PL quenching for both of them, while the $\bullet O_2^-$-derived HTLs exhibit lower PL intensity than that of LiTFSI-doped ones, suggesting the excellent hole extraction ability of the $\bullet O_2^-$-derived spiro-OMeTAD. Similarly, as observed in Fig. 3e, the average carrier decay lifetime is reduced from 77.5 ns to 21.9 ns for the perovskite/$\bullet O_2^-$-derived HTLs (Supplementary Table 2). These results indicate that the hole extraction at the perovskite and HTL interface has been significantly enhanced, most likely as a result of interfacial energy level optimization. Ultraviolet photoelectron spectroscopy (UPS) was thus performed to investigate the impact of O_2^- on the relevant energy levels (Supplementary Fig. 8). The energy of the highest occupied molecular orbital (HOMO) is calculated to be −5.01 and −5.19 eV for LiTFSI-doped and O_2^--derived HTLs, respectively. The interfacial band alignment using different HTLs could be depicted with the corresponding energy-level diagram (Fig. 3f). The optimized energy level of the $\bullet O_2^-$-derived HTLs lowers

https://doi.org/10.1038/s41467-024-52199-4

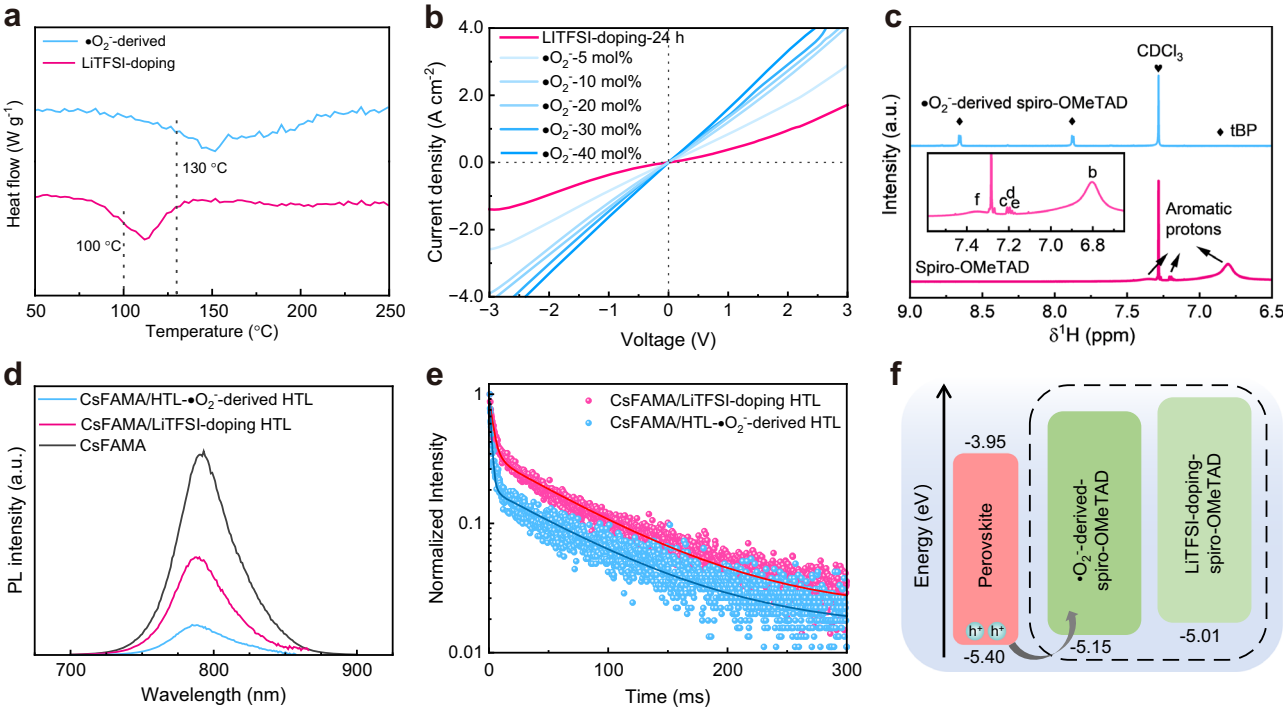

Fig. 3 | The characterization of the $\bullet O_2^-$-derived spiro-OMeTAD. a DSC curves of the LiTFSI-doped and $\bullet O_2^-$-derived spiro-OMeTAD. The vertical dashed lines indicate the glass transition temperature. **b** *J-V* curves for the LiTFSI-doped spiro-OMeTAD (oxidation for 24 h) and the $\bullet O_2^-$-derived spiro-OMeTAD with different concentration of $Eu(TFSI)_2$, respectively. **c** ^1H NMR characterization of the spiro-OMeTAD solution with or without $\bullet O_2^-$ doping (4-tert-butylpyridine, tBP; deuterated chloroform, $CDCl_3$). Steady-state PL (**d**) and TRPL (**e**) spectra for CsFAMA perovskite and CsFAMA/spiro-OMeTAD HTL (doped by LiTFSI and $\bullet O_2^-$) films. **f** Schematic diagram of energy levels for perovskite films with different HTLs. Source data are provided as a Source Data file.

the interfacial charge transfer barrier, facilitating hole extraction and minimizing carrier recombination. This, in return, enhances photovoltaic performance of PSCs, especially with respect to achieving a high open-circuit voltage (V_{OC}).

Photovoltaic performance of PSCs upon $\bullet O_2^-$-doped spiro-OMeTAD HTLs

In order to explore the effects of $\bullet O_2^-$-doped HTLs on photovoltaic performance, a series of n-i-p planar PSCs were constructed using various O_2^--derived spiro-OMeTAD HTLs deposited on perovskite films with the composition of $Cs_{0.05}FA_{0.85}MA_{0.10}PbI_{2.91}Br_{0.09}$ (CsFAMA, bandgap of 1.56 eV, Supplementary Fig. 9). The corresponding configuration of FTO/TiO_2/perovskite/spiro-OMeTAD/Au is shown in Fig. 1a. The optimum doping concentration of spiro-OMeTAD HTLs for CsFAMA devices is 40 mol%, as indicated by the statistics of 40 individual devices under each condition in Figs. 4a–c and Supplementary Fig. 10, and the corresponding photovoltaic metrics were summarized in Supplementary Table 3. The average PCEs rise increasingly from LiTFSI-doped 22.40% to 25.06%, attributed to the large improvement of V_{OC} (from 1.161 to 1.205 V) and fill factor (FF, from 77.89% to 82.01%), as well as the slight increase of short-circuit current density (J_{SC}, from 24.77 mA cm^{-2} to 25.36 mA cm^{-2}). As shown in current density-voltage (*J-V*) curves in Fig. 4d and Table 1, the O_2^--derived CsFAMA devices yield immediately a champion PCE of 25.45% under reverse scanning, with V_{OC} of 1.210 V, J_{SC} of 25.41 mA cm^{-2}, and FF of 82.50%, based on the optimized concentration. However, conventional LiTFSI-doped devices achieve a PCE of merely 23.19% under reverse scanning after oxidation for over 24 hours. More importantly, the O_2^--derived devices exhibit a negligible hysteresis (hysteresis index (HI), 0.04%) when measured in both reverse and forward scanning (Table 1), which is significantly smaller than that of the LiTFSI-doped devices (6.0%). Additionally, the $\bullet O_2^-$-derived devices deliver a stabilized power output (SPO) of 25.22% for 100 s, while the SPO of LiTFSI-doped devices is just stabilized at 22.48% (Supplementary Fig. 11). It should be noted that the PCE of 25.45% is one of the highest value recorded to date for PSCs based on Li-free and post-oxidation-free spiro-OMeTAD HTLs (Fig. 4e and Supplementary Table 1). Supplementary Fig. 12 shows the corresponding EQE spectra of the champion CsFAMA devices with an integrated current density of 24.28 mA cm^{-2} for LiTFSI-doped PSCs and 24.70 mA cm^{-2} for $\bullet O_2^-$-derived PSCs, respectively, which are in good agreement with the *J-V* results. The enhanced EQE in the long wavelength range of 650–780 nm is mainly attributed to the optimized energy-level arrangement at the interface between perovskite and $\bullet O_2^-$-derived spiro-OMeTAD. In order to demonstrate the applicability and compatibility of the $\bullet O_2^-$-derived spiro-OMeTAD HTLs on large-area perovskite films, a 6 × 6 cm^2 PSC module with an active area of 18 cm^2 was fabricated (see details in "Methods" section). Similar to the small-area PSCs, this module achieves a remarkable PCE of 20.35% (average value from reverse and forward scan results) with negligible hysteresis, (Fig. 4f and Table 1). These results indicate the universality and upscaling capacity of the $\bullet O_2^-$-derived spiro-OMeTAD HTLs on enhancing photovoltaic performance regardless of the device areas.

To enhance comprehension of the mechanism by which photovoltaic performance improves, Fig. 4g illustrates the relationship between V_{OC} and light intensity. The deviation of the slope from k_BT/q reflects defect-assisted recombination in PSCs, where k_B denotes the Boltzmann constant, T represents the absolute temperature, and q is the electric charge. It is found that the LiTFSI-doped devices exhibit a significantly steeper 1.72 k_BT/q in comparison to those doped with the $\bullet O_2^-$-derived devices (1.47 k_BT/q). This indicates substantially reduced carrier recombination within PSCs, which results from the decreased charge extraction barrier at the interface between perovskite and $\bullet O_2^-$-derived spiro-OMeTAD. This is also evident from the electrical impedance spectroscopy (EIS) in Fig. 4h. According to the fitting results of two Nyquist plots, the LiTFSI-doped devices show a charge transport resistance (R_{ct}) of 6039 Ω at high-frequency, as well as a charge

https://doi.org/10.1038/s41467-024-52199-4

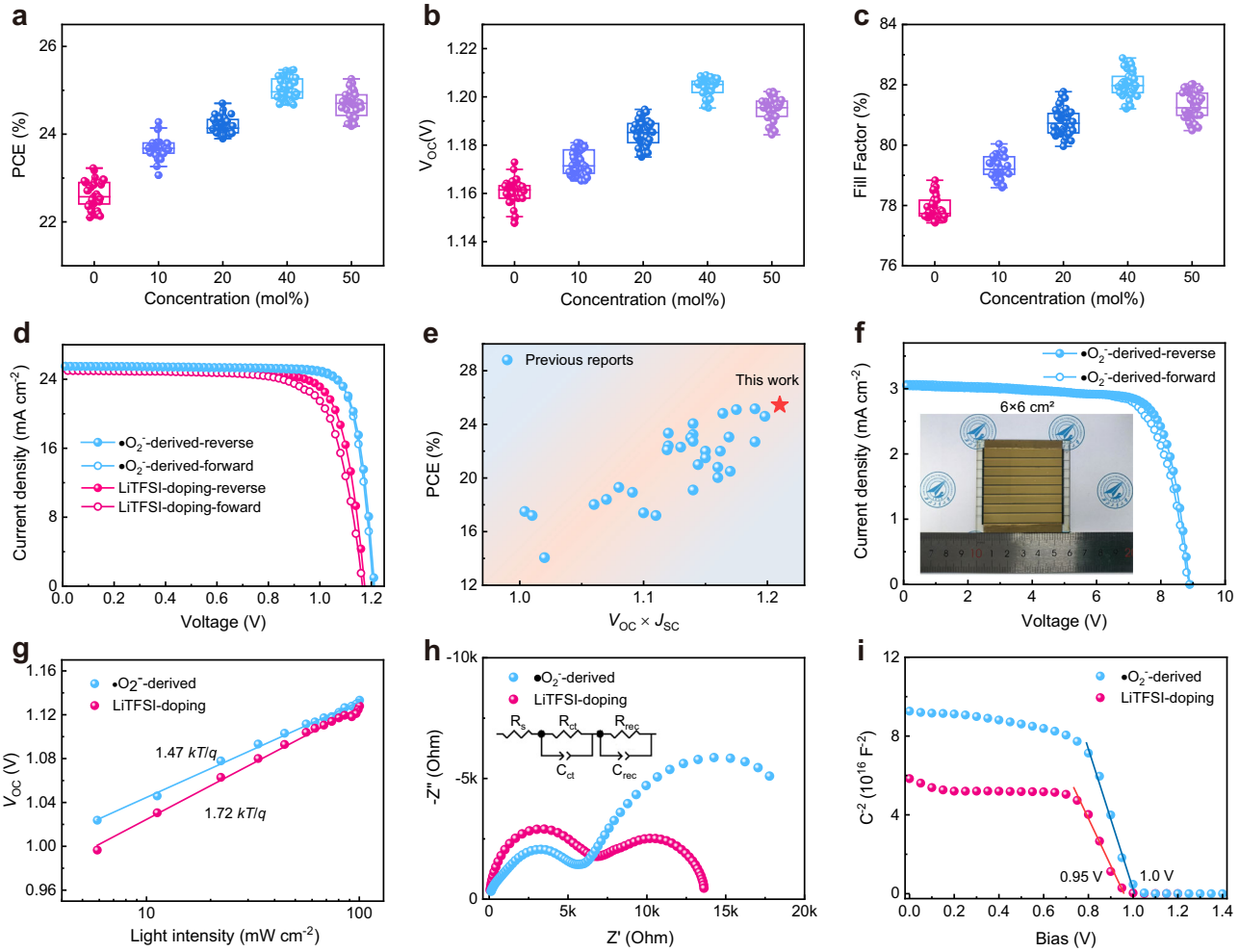

Fig. 4 | Performance of PSCs employing different HTLs. Statistical distribution of 40 individual CsFAMA devices with different •O_2^--derived spiro-OMeTAD HTLs: **a** PCE, **b** V_{OC}, **c** FF. **d** *J-V* curves of champion CsFAMA devices with LiTFSI-doped and •O_2^--derived spiro-OMeTAD HTLs under reverse scan and forward scan, respectively. The insets in (**d**, **e**) are stabilized power outputs of the corresponding devices. **e** Summary of the reported PCE of the recently reported PSCs based on modified spiro-OMeTAD HTLs. **f** *J-V* curves of the 6 × 6 cm² PSC module with •O_2^--derived spiro-OMeTAD HTLs under reverse scan and forward scan. **g** V_{OC} vs light intensity curves for PSCs with different HTLs. **h** Nyquist plots of PSCs with different HTLs in dark. **i** Mott-Schottky plots of PSCs with different HTLs. Source data are provided as a Source Data file.

Table 1 | Photovoltaic parameters of PSCs employing different spiro-OMeTAD HTLs

Devices	Scanning mode	V_{OC} (V)	J_{SC} (mA cm^{-2})	FF (%)	PCE (%)
LiTFSI-doping	Reverse	1.174	25.05	78.87	23.19
	Forward	1.166	25.00	74.77	21.80
•O_2^--derived (0.05 cm²)	Reverse	1.210	25.49	82.50	25.45
	Forward	1.209	25.54	82.47	25.46
•O_2^--derived (6 × 6 cm²)*	Reverse	8.910	3.05	76.40	20.76
	Forward	8.880	3.07	75.08	20.47

* Note: the active area is 18 cm².

recombination resistance (R_{rec}) of 1.09×10^5 Ω at low-frequency. While the •O_2^--derived devices present lower R_{ct} of 5460 Ω and higher R_{rec} of 1.89×10^5 Ω, indicating efficient charge collection and reduced recombination in PSCs. Additional evidence of this reduced interface barrier was further confirmed by the Mott-Schottky (M-S) plots shown in Fig. 4i. The slope of M-S plots inversely reflects the interfacial charge density of PSCs[30], which is calculated to be 0.85×10^{16} cm^{-3} and 1.34×10^{16} cm^{-3} for the •O_2^--derived and LiTFSI-doped devices, respectively. Furthermore, the •O_2^--derived devices demonstrate an increased built-in potential from pristine 0.95 V to 1.0 V, which is also benefit for the enhancement of V_{OC} and SPO for PSCs. These results indicate that rapid charge collection and reduced carrier accumulation at the interface between perovskite and •O_2^--derived spiro-OMeTAD, along with the boosted conductivity of spiro-OMeTAD layer, contribute to high PCE of PSCs with significantly increased V_{OC} and FF.

Environmental stability of PSCs upon •O_2^--derived spiro-OMeTAD HTLs

The storage stability of different spiro-OMeTAD films was first explored at room temperature under a relative humidity (RH) of 40% (a

https://doi.org/10.1038/s41467-024-52199-4

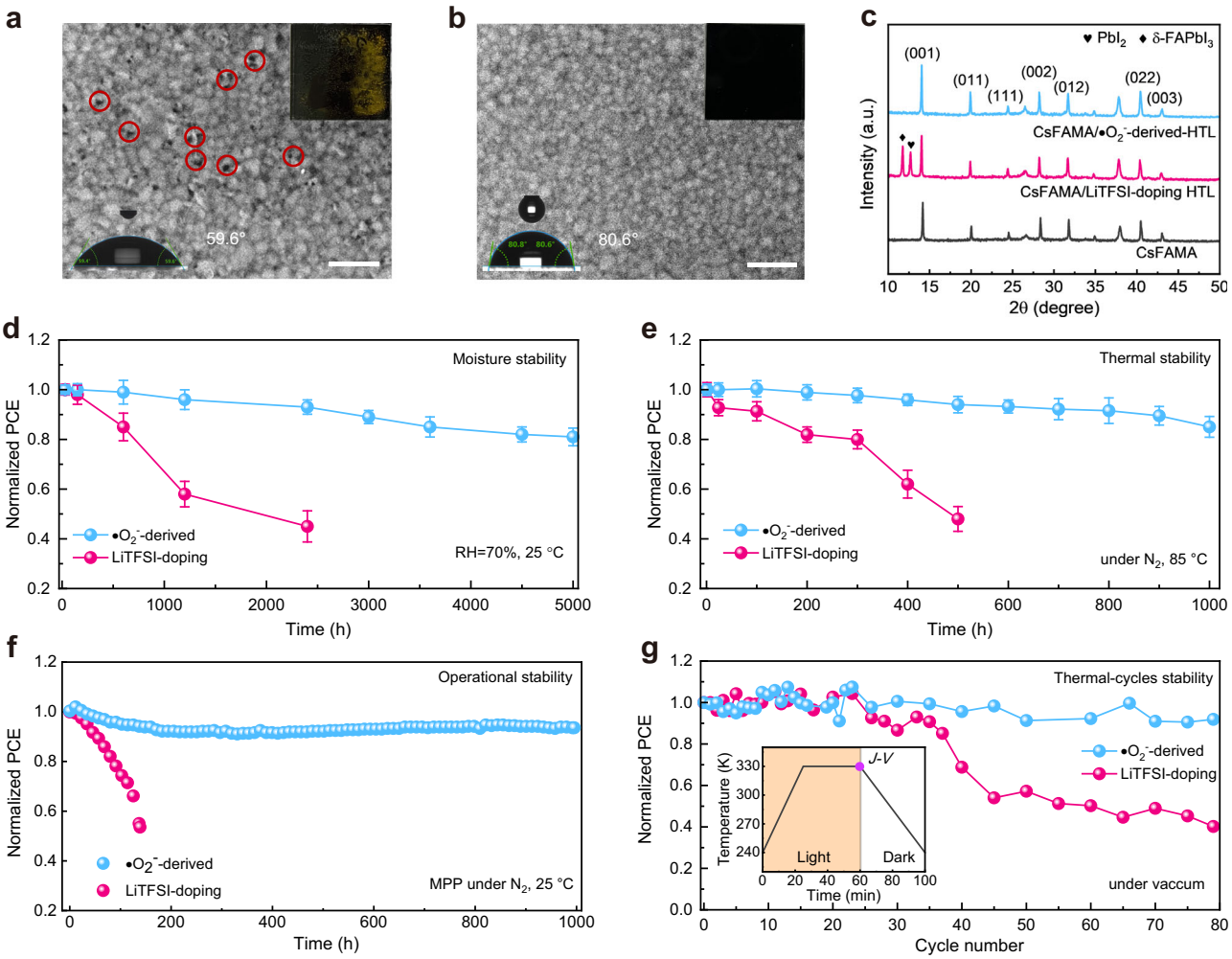

Fig. 5 | Stability of PSCs under various conditions. SEM images of different spiro-OMeTAD HTLs deposited on perovskite films after aging in air with 70% RH for 1000 h: **a** LiTFSI-doping, **b** $\bullet O_2^-$-derived. The scale bar is 2 μm and the insets (left) in (**a**,**b**) are corresponding contact angle tests, and the insets (right) in (**a**,**b**) are corresponding optical images. **c** XRD patterns of different HTLs deposited on perovskite films before and after aging in air with 70% RH for 1000 h. CsFAMA pattern is included as reference for comparison. **d** Moisture stability of unencapsulated CsFAMA PSCs with different HTLs aged in air (70% of RH, 25 °C). **e** Thermal stability of CsFAMA PSCs with different HTLs under heating stress (85 °C) in an inert atmosphere. The error bars in (**d**) and (**e**) represent the standard deviation for 5 devices. **f** Operational stability of CsFAMA PSCs with different HTLs under continuous illumination (100 mW cm^{-2}) under inert atmosphere. **g** Light-thermal cycling stability of CsFAMA PSCs with different HTLs under simulated LEO conditions (see the inset in (**g**)). Source data are provided as a Source Data file.

general oxidation environment for regular PSCs; see Supplementary Fig. 5). Prior to aging, all spiro-OMeTAD films deposited on FTO glass substrates exhibit flat, compact, and clean morphologies, regardless of the doping method. However, some precipitated phases emerge in LiTFSI-doped spiro-OMeTAD after only 24 hours of oxidation. This is due to the hygroscopicity and migration of Li salts. These phases further increase and evolve over the course of 10 months of air exposure. In contrast, $\bullet O_2^-$-derived spiro-OMeTAD is capable of maintaining its initial morphology during long-term aging. The moisture stability of perovskite films was evaluated by depositing different spiro-OMeTAD HTLs onto them under RH of 70%. As shown in Figs. 5a and 5b, the LiTFSI-doped samples show numerous pinholes after 1000 hours, which further deteriorate under harsh conditions (85% RH and 85°C, Supplementary Fig. 13). These pinholes create pathways for moisture in the air to diffuse through the HTL and degrade the perovskite underneath, whereas the $\bullet O_2^-$-derived samples remain unchanged under such harsh conditions. This indicates that the hydrophobicity of the $\bullet O_2^-$-derived samples has been improved owing to the absence of Li, thereby inhibiting the moisture infiltration, as evidenced by the increased contact angle from 59.6° to 80.6° (see the insets in Figs. 5a, b). Such protection contributes thus to the improved moisture stability of the perovskite films, evidenced by the color changes of the perovskite films (see the insets in Figs. 5a and 5b). The degradation of perovskite films with different HTLs under a RH of 70% was checked using X-ray diffraction (XRD) analysis, as shown in Fig. 5c. It is found that two distinct peaks emerged at 11.6° and 12.7° in LiTFSI-doped samples after 1000 hours, which correspond to the δ-phase perovskite and PbI_2. While the $\bullet O_2^-$-derived samples demonstrate excellent moisture stability as indicated by the absence of phase change and displacement of diffraction peaks.

We further investigated the environmental stability of the corresponding PSCs on the basis of the stability analyzes of perovskite films with different HTLs. Firstly, the moisture stability of unencapsulated PSCs was evaluated in ambient air under an RH of 70%. As shown in Fig. 5d, the PCEs of the LiTFSI-doped devices exhibit a consistent decline, reaching 45% of their initial PCE after 2400 hours. Whereas the $\bullet O_2^-$-derived devices retain more than 80% of their initial efficiency even after 5000 hours. Surprisingly, the thermal stability of $\bullet O_2^-$-derived devices shows an even more significant improvement. As shown in Fig. 5e, the $\bullet O_2^-$-derived devices retain 90% of their initial PCE after annealing at 85°C for 1000 hours, while LiTFSI-doped devices retain only 48% of their initial PCE after 500 hours. The remarkable

enhancement observed can be attributed to the utilization of Li-free doping and the exceptional thermal stability exhibited by the $•O_2^-$-derived spiro-OMeTAD HTLs (Fig. 3a). The operational stability of PSC devices with different HTLs was tracked over time at the maximal power point (MPP) under continuous light (100 mW cm^{-2}). As shown in Fig. 5f, the $•O_2^-$-doped devices exhibit superior operational stability, maintaining 95% of their initial PCE for 1000 hours in comparison with that of LiTFSI-doped devices (50% for 150 h).

Furthermore, recent reports have demonstrated that PSCs can endure the extreme environmental conditions of space, such as electron/proton radiation, gamma ray, and UV light exposure[31–33]. In space-based PSCs, however, the effect of thermal cycling in conjunction with light exposure has not been thoroughly investigated. Therefore, we investigated the effect of light-thermal cycles on the PCE of the $•O_2^-$-derived devices under simulated conditions of LEO (see the inset in Fig. 5g and "Methods" section). As shown in Fig. 5g, the PCE derived from the *J-V* curves taken at 330 K is plotted for 80 LEO cycles, and the corresponding photovoltaic parameters (J_{SC}, V_{OC} and FF) are summarized in Supplementary Fig. 14. It can be observed that the $•O_2^-$-derived devices show higher stability, maintaining 90% of their initial PCE after 80 LEO cycles. On the contrary, the LiTFSI-doped devices retain only 40% of their initial PCE after an equivalent of 80 LEO cycles. This indicates that the $•O_2^-$-derived HTLs endure the erosion caused by light-thermal cycles under LEO conditions, indicating their potential in near-space and polar region applications. In fact, a comparison of the dark *J-V* curves before and after the LEO experiment reveals that the $•O_2^-$-doped devices exhibit significantly fewer degradation in diode characteristics (Supplementary Fig. 15).

It is important to emphasize that present work demonstrates the feasibility of spiro-OMeTAD pre-oxidization in solution through the construction of $•O_2^-$ using the variant-valence $Eu(TFSI)_2$ salts for highly efficient and stable PSCs. As the $•O_2^-$ is more reactive than molecular oxygen (O_2) due to differences in their electronic structures (Supplementary Note 2)[34,35], the entire oxidization process can thus be completed within 30 seconds and rapidly promote the p-type doping of spiro-OMeTAD, along with instantly increased conductivity and work function of their HTLs. In addition, it is worth noting that the absence of hygroscopic LiTFSI in the $•O_2^-$-derived spiro-OMeTAD solution, along with the ultrafast oxidation process in air, could contribute to minimizing the impact of the external environment (Supplementary Fig. 16). To assess the impact of temperature on the doping rate of spiro-OMeTAD HTLs as well as the efficiency and stability of PSCs, additional experiments were conducted by bubbling O_2 into spiro-OMeTAD:$Eu(TFSI)_2$ solutions at various temperatures (0°C, 23°C, 40°C, 60°C, and 85°C). The results revealed a gradual increase in the oxidation rate of the spiro-OMeTAD solution with higher temperatures. However, over a sufficient period of time, the degree of oxidation reached consistent levels (see the final color at 40°C, 60°C and 85°C in Supplementary Movie 4 and Supplementary Fig. 17), indicating the amount of formed $•O_2^-$ at different temperatures is identical. These results suggest that the final amount of formed $•O_2^-$ is predominantly influenced by the concentration of $Eu(TFSI)_2$ introduced and the duration of oxygen exposure. Therefore, it is expected that the doping of spiro-OMeTAD HTLs and the performance of their devices would not be affected by the applied temperatures (Supplementary Fig. 18, Supplementary Table 4 and Supplementary Note 6).

Owing to the interfacial energy-level optimization between perovskite and spiro-OMeTAD, the $•O_2^-$-derived devices achieve remarkable photovoltaic performance with PCEs of over 25% in a small area (0.05 cm^2) and over 20% in a 6 × 6 cm^2 module (active area, 18 cm^2). Furthermore, the hysteresis observed during the *J-V* scan is negligible. More importantly, in the absence of lithium, devices doped with $•O_2^-$ demonstrate substantially enhanced stability when subjected to external stimuli such as moisture, heat, light, and even thermal-light cycling. This is primarily due to the increased T_g and hydrophobicity as well as the suppressed ionic migration for HTLs. As far as we know, both the efficiency and stability of the current $•O_2^-$-derived device rank among the top records in PSCs based on the post-oxidation-free and Li-free spiro-OMeTAD HLTs (Supplementary Table 1). It is also worth noting that the extracted $•O_2^-$-derived spiro-OMeTAD powder (the insets of Fig. 2e) could be used directly as the precursor to deposit HTLs without any additional treatments, delivering nearly identical PCE regardless of the storage time compared to that of its solution counterpart (Supplementary Fig. 16). Given these striking merits, we believe such $•O_2^-$-deriving strategy for metal-free HTLs will be inspiring for researchers working on low-cost and shortened processing of n-i-p PSCs employing spiro-OMeTAD as HTLs (Supplementary Note 7), which is particularly crucial for the commercialization and scaling-up of perovskite photovoltaics.

In summary, we have demonstrated an efficient Li-free and post-oxidation-free doping strategy to address the environmental instability of the spiro-OMeTAD HTLs by constructive $•O_2^-$ with strong oxidation capability, minimizing the trade-off between high efficiency and high stability of n-i-p PSCs. Such doping can be facilely realized in the as-prepared spiro-OMeTAD solution within 30 s by adding of variant-valence Eu^{2+} salts, and instantly obtain high conductivity and ideal work function when depositing as HTLs without additional post-treatments. Thus, the fabricated PSCs based on such HTLs universally feature not only high efficiency in different active areas that can rival the performance of the state-of-the-art LiTFSI-doped PSCs, but deliver excellent stability under various external stimuli. The $•O_2^-$-deriving strategy in present work provides possibilities to advance the development of commercialization for regular perovskite photovoltaics.

Methods

Materials

Unless stated otherwise, all materials were purchased from Sigma-Aldrich without further purification. Fluorine-doped tin oxide (FTO) coated glass substrates with partial etching were purchased from Opvtech. Formamidine iodide (FAI, 99.5%), methylamine hydrobromide (MABr, 99.9%), cesium iodide (CsI, ≥ 99.9%), lead bromide ($PbBr_2$, ≥ 99.9%), lead iodide (PbI_2, 99.99%), spiro-OMeTAD (≥ 99.8%), 4-tert-butylpyridine (tBP, ≥ 99.9%) and lithium-bis(trifluoromethanesulfonyl)imide (LiTFSI, ≥ 99.9% purity) were purchased from Xi'an Polymer Light Technology Corp. Bis(trifluoromethanesulfonyl)imide (HTFSI, 99% purity) were purchased from Innochem Technology Corp. Titanium tetrachloride ($TiCl_4$) were purchased from Alfa Aesar.

Preparation of $Eu(TFSI)_2$ solution

$Eu(TFSI)_2$ solution was prepared by adding 300 mg of HTFSI and excess Europium (Eu, 99% purity) in 1 mL acetonitrile solvent in a nitrogen-filled glovebox, the bubbles could be observed instantly, demonstrating strong chemical reactions between Eu and HTFSI. After reaction, the formed $Eu(TFSI)_2$ solution was filtered using an organic filter (0.22 μm, PTFE), and then stored in brown bottles in a nitrogen-filled glovebox. The $Eu(TFSI)_2$ precursor solution is very stable in the inert atmosphere for more than several months and can be used directly without re-filtration.

Preparation of spiro-OMeTAD precursor solution

The classic LiTFSI-doped spiro-OMeTAD precursor solution was prepared by dissolving 72 mg spiro-OMeTAD, 28.5 μL tBP and 17.5 μL LiTFSI solution (520 mg mL^{-1} in acetonitrile) in 1 mL chlorobenzene (CB) in N_2 glovebox, and then stirred and filtered (0.22 μm, PTFE) before use.

For the $•O_2^-$-derived spiro-OMeTAD, $Eu(TFSI)_2$ with different mole ratios to spiro-OMeTAD including 0.05:1,0.10:1, 0.20:1, 0.30:1, 0.40:1, and 0.50:1, along with 15 μL tBP that was employed to improve the

dispersibility of $Eu(TFSI)_2$[36], were added into the spiro-OMeTAD:CB solution, respectively. The mixtures were then bubbled with O_2 for different durations. The optimal mole ratio of $Eu(TFSI)_2$ to spiro-OMeTAD was determined to be 0.40:1. After filtration (0.22 μm, PTFE), the oxidized spiro-OMeTAD solution was consequently obtained, and can be directly deposited as the HTL of Li-free spiro-OMeTAD for PSCs, without the need for a post-oxidation process. Also, the pre-oxidized spiro-OMeTAD solution can be extracted as powders through facile drying. These spiro-OMeTAD powders can then be redissolved and deposited as HTLs for PSCs without any additional treatments.

Device fabrication

The FTO glass was cleaned in detergent, deionized water, acetone and isopropanol sequentially. After drying by N_2 blowing, the cleaned FTO substrates were treated with ultraviolet ozone for 20 min. An ~40 nm thick TiO_2 compact layer was prepared by chemical bath deposition[37,38]. In brief, 0.8 mL $TiCl_4$ was first added drop by drop to 40 mL of ice water. After the melt of the ice, the clean FTO glass was then immersed in the $TiCl_4$ aqueous solution using a petri dish as the vessel, and heated at 70°C for 60 min in an oven. After washing with pure water, the TiO_2 films were prepared onto FTO glass by nitrogen purging and further heat treatment at 100°C for 30 min. The FTO/TiO_2 substrate was treated with ultraviolet ozone for 10 min before deposition of the perovskite film. The $Cs_{0.05}FA_{0.85}MA_{0.10}PbI_{2.91}Br_{0.09}$ precursor solution (1.55 M) was obtained by dissolving CsI (20.13 mg), FAI (226.57 mg), PbI_2 (750.31 mg), MABr (17.36 mg), and MACl (20.93 mg) in a mixed solvent (DMF/DMSO = 4:1). The resulting solution was coated onto the FTO/TiO_2 substrate by a consecutive two-step spin-coating process at 2000 and 4000 r.p.m for 10 and 30 s, respectively. Then, 0.2 mL ethyl acetate was immediately poured on the spinning substrate 10 s prior the end of the program. Thereafter, the substrate was placed onto a hotplate for 60 min at 100°C.

For the hole transporting layer, 20 μL different spiro-OMeTAD precursor solutions were deposited onto the top of the perovskite layer by spin-coating at 4000 rpm for 30 s. Finally, 100 nm of Au electrode was thermally evaporated on the hole transporting layer using a shadow mask. The active area of this electrode was 0.05 cm^2, which was calculated by a mask plate and further determined by an optical microscope.

For the fabrication of 6 × 6 cm^2 PSC modules, three laser-patterning lines, P1 (200 μm), P2 (200 μm), and P3 (400 μm), were created using a laser beam with power settings of 18 W, 10 W, and 7 W, respectively[39]. And the thermal-stable FACs perovskite was used to prepare the module. The FACs perovskite precursor is a mixture solution of PbI_2 (461 mg), FAI (163.4 mg), $PbCl_2$ (19.2 mg), MACl (20 mg), CsI (13 mg) in 600 μL DMF and 90 μL NMP. The large-scale perovskite layers were prepared by the blade coating and a vacuum-flash process. The gap between the blade and the FTO/TiO_2 was about 200 μm and the speed of the blade was 5 mm s^{-1}. The resultant wet film was shifted into a vacuum system (~10 Pa) to quickly remove solvent, and then was shifted onto a hotplate at 130°C for 10 min. Then, the spiro-OMeTAD HTL and Au electrode were successively deposited onto the perovskite layer by spin-coating and thermal evaporation, respectively.

Characterization

Under standard AM 1.5 G illumination using a xenon-lamp-based solar simulator (Enlitech, IVS-KA5000), the current-voltage (*J-V*) characteristic and steady-state power output of solar cells were measured by a Keithley 2420 Source Meter. The light intensity was calibrated by a silicon (Si) diode (Hamamatsu S1133) equipped with a Schott visible-color glass filter (KG5 color-filter). The step voltage and scan speeds were 20 mV and 0.2 V s^{-1}. A mask with size of 0.04556 cm^2 was used to calculate the current density of PSCs during testing. EQE measurement was carried out with a Newport QE measurement kit by focusing a monochromatic beam of light onto the devices.

SEM images were obtained using a field emission scanning electron microscope (FEI Verios G4). The absorption was characterized by the ultraviolet-visible (UV-vis) spectrophotometer (Perkin-Elmer Lambda 35 UV-vis-NIR). The FTIR spectra (4000–500 cm^{-1}) were recorded on a Jasco FT/IR-6100 FTIR. The X-ray diffraction (XRD) spectra were obtained by a PANAlytical X'pert PRO. The X-ray photoelectron spectroscopy (XPS) measurements were carried out by an Axis Supra (Kratos). The Thermogravimetric analysis and differential scanning calorimetry were performed on Netzsch STA-2500 at a heating rate of 10 °C min^{-1} under nitrogen atmosphere. Electron Paramagnetic Resonance (EPR) spectra were acquired with a Bruker A300 spectrometer. The generation of superoxide radical anion $\bullet O_2^-$ in CB was studied using EPR spectroscopy and 5, 5-dimethyl-1-pyrroline-N-oxide (DMPO) as spin trap. High-resolution liquid nuclear magnetic resonance (NMR) spectra were acquired with a Bruker Avance 500 spectrometer operating at 500 MHz for 1H. Samples were dissolved in deuterated chloroform ($CDCl_3$) solvent mixture. Ultraviolet photoelectron spectroscopy (UPS) was characterized by a VG Scienta R4000 analyzer and the HeI (21.22 eV) emission line employed for excitation at a bias of -5V. The contact angles measurements were conducted by a data physics OCA-20 contact-angle system at ambient air. The steady-state photoluminescence spectra were obtained using a pulse laser as an optical excitation source (wavelength: 470 nm, Horiba FluorologFL-3), and a time-resolved photoluminescence (TRPL) experiment was carried out by excitation at 470 nm. The electrical impedance spectroscopy (EIS) was characterized applying a bias of 0.8 V in the dark in a frequency range from 1 MHz to 0.1 Hz (CHI660E). The active area of the device in the EIS measurement is 0.05 cm^2. Mott-Schottky was measured by a CHI660E at a frequency of 1 kHz with an applied bias voltage of 0 V ~ 1.4 V.

Moisture-stability measurements of the non-encapsulated films/solar cells were performed in a constant temperature and humidity incubator in dark. Thermal-stability of the non-encapsulated solar cell was tested on a hot plate (85°C) in a nitrogen atmosphere. PCEs of the devices were periodically measured under AM1.5 G simulated sun light in ambient air. Long-term operational stability of the non-encapsulated devices were measured under MPP tracking and continuous light irradiation with a white LED lamp, 100 mW cm^{-2} in a nitrogen atmosphere.

For the simulated low earth orbit (LEO) test, the devices were placed in a cryostat chamber under a 3×10^{-5} mbar vacuum environment. The temperature and time were controlled with a custom-made Labview program to mimic the conditions of a spacecraft in LEO. During the LEO cycle the device was initially exposed to sunlight at 240 K, and the temperature was increased at a constant rate up to 330 K during 40 min, under continuous light exposure. Then, after 20 min of light exposure at 330 K, the light source was switched off and the temperature was decreased at a constant rate down to 240 K during 30 min. From this point, the cycle was started again. The LEO cycles were performed using a Xe light source equipped with an AM1.5 G solar filter yielding a power density of 100 mW·cm^{-2} at the device, calibrated with a pyroelectric radiometer. A K230 Keithley voltage source as well as a K617 Keithley electrometer was used to perform the *J-V* measurements. The *J-V* curves were taken at 330 K at the end of the illumination period, sweeping the voltage from reverse to forward bias at a rate of 10 mV s^{-1}, with 0.01 V step, and 300 ms of delay between points, and no preconditioning conditions were applied. The devices were biased at MPP conditions during illumination, and were left under open circuit under dark conditions.

Reporting summary

Further information on research design is available in the Nature Portfolio Reporting Summary linked to this article.

Data availability

The authors declare that the data supporting the findings of this study are available within the article and its Supplementary Information files. Additional details that support the findings of this study will be made available by the corresponding author upon request. Source data are provided with this paper.

References

1. Zhang, T. et al. Ion-modulated radical doping of Spiro-OMeTAD for more efficient and stable perovskite solar cells. *Science* **377**, 495–501 (2022).
2. Yang, H. et al. Iodonium initiators: Paving the air-free oxidation of Spiro-OMeTAD for efficient and stable perovskite solar cells. *Angew. Chem. Int. Ed.* **63**, 202316183 (2024).
3. Zhao, Y. et al. Inactive $(PbI_2)_2RbCl$ stabilizes perovskite films for efficient solar cells. *Science* **377**, 531–534 (2022).
4. Kong, J. et al. CO_2 doping of organic interlayers for perovskite solar cells. *Nature* **594**, 51–56 (2021).
5. Liu, X. et al. Perovskite solar cells based on Spiro-OMeTAD stabilized with an alkylthiol additive. *Nat. Photonics* **17**, 96–105 (2023).
6. Abate, A. et al. Lithium salts as "redox active" p-type dopants for organic semiconductors and their impact in solid-state dye-sensitized solar cells. *Phys. Chem. Chem. Phys.* **15**, 2572–2579 (2013).
7. Wang, S. et al. Role of 4-tert-butylpyridine as a hole transport layer morphological controller in perovskite solar cells. *Nano Lett.* **16**, 5594–5600 (2016).
8. Wang, S., Yuan, W. & Meng, Y. S. Spectrum-dependent Spiro-OMeTAD oxidization mechanism in perovskite solar cells. *ACS Appl. Mater. Interfaces* **7**, 24791–24798 (2015).
9. Zhao, W. et al. Laser derived electron transport layers with embedded p-n heterointerfaces enabling planar perovskite solar cells with efficiency over 25%. *Adv. Mater.* **35**, 2300403 (2023).
10. Cappel, U. B., Daeneke, T. & Bach, U. Oxygen-induced doping of Spiro-OMeTAD in solid-state dye-sensitized solar cells and its impact on device performance. *Nano Lett.* **12**, 4925–4931 (2012).
11. Forward, R. L. et al. Protocol for quantifying the doping of organic hole-transport materials. *ACS Energy Lett.* **4**, 2547–2551 (2019).
12. Kim, S. G. et al. Capturing mobile lithium ions in a molecular hole transporter enhances the thermal stability of perovskite solar cells. *Adv. Mater.* **33**, 2007431 (2021).
13. Chen, H. W. et al. A switchable high-sensitivity photodetecting and photovoltaic device with perovskite absorber. *J. Phys. Chem. Lett.* **6**, 1773–1779 (2015).
14. Jeong, M. et al. Stable perovskite solar cells with efficiency exceeding 24.8% and 0.3-V voltage loss. *Science* **369**, 1615–1620 (2020).
15. Boyd, C. et al. Understanding degradation mechanisms and improving stability of perovskite photovoltaics. *Chem. Rev.* **119**, 3418–3451 (2019).
16. Jeon, N. J. et al. A fluorene-terminated hole-transporting material for highly efficient and stable perovskite solar cells. *Nat. Energy* **3**, 682–689 (2018).
17. Webb, T. et al. A multifaceted ferrocene interlayer for highly stable and efficient lithium doped Spiro-OMeTAD-based perovskite solar cells. *Adv. Energy Mater.* **12**, 2200666 (2022).
18. Li, Z. et al. Extrinsic ion migration in perovskite solar cells. *Energy Environ. Sci.* **10**, 1234–1242 (2017).
19. Wu, J. et al. Directly purifiable pre-oxidation of Spiro-OMeTAD for stability enhanced perovskite solar cells with efficiency over 23%. *Chem. Eng. J.* **437**, 135457 (2022).
20. Seo, J. Y. et al. Dopant engineering for Spiro-OMeTAD hole-transporting materials towards efficient perovskite solar cells. *Adv. Funct. Mater.* **31**, 2102124 (2021).
21. Seo, J. Y. et al. Novel p-dopant toward highly efficient and stable perovskite solar cells. *Energy Environ. Sci.* **11**, 2985–2992 (2018).
22. Tan, B. et al. LiTFSI-free Spiro-OMeTAD-based perovskite solar cells with power conversion efficiencies exceeding 19%. *Adv. Energy Mater.* **9**, 1901519 (2019).
23. Nguyen, W. et al. Enhanci tnghe hole-conductivity of Spiro-OMeTAD without oxygen or lithium salts by using spiro$(TFSI)_2$ in perovskite and dye-sensitized solar cells. *J. Am. Chem. Soc.* **136**, 10996–11001 (2014).
24. Abate, A. et al. Protic ionic liquids as p-dopant for organic hole transporting materials and their application in high efficiency hybrid solar cells. *J. Am. Chem. Soc.* **135**, 13538–13548 (2013).
25. Shen, Y. et al. Crowning lithium ions in hole-transport layer toward stable perovskite solar cells. *Adv. Mater.* **34**, 2200978 (2022).
26. Yang, L. et al. Enhancement of oxygen/pressure sensing performance of Eu^{3+}-doped YSZ phosphors via Bi^{3+} sensitization. *Ceram. Int.* **48**, 31587 (2022).
27. Dvoranova, D., Barbieriková, Z. & Brezová, V. Radical intermediates in photoinduced reactions on TiO_2 (An EPR spin trapping study). *Molecules* **19**, 17279–17304 (2014).
28. Zhang, F. et al. Engineering of hole transporting interface by incorporating the atomic-precision Ag_6 nanoclusters for high-Efficiency blue perovskite light-emitting diodes. *Nano Lett.* **23**, 1582–1590 (2023).
29. Olthof, S. et al. Ultralow doping in organic semiconductors: Evidence of trap filling. *Phys. Rev. Lett.* **109**, 176601 (2012).
30. Bu, T. et al. Universal passivation strategy to slot-die printed SnO_2 for hysteresis-free efficient flexible perovskite solar module. *Nat. Commun.* **9**, 4609 (2018).
31. Chen, Y. et al. Self-elimination of intrinsic defects improves the low-temperature performance of perovskite photovoltaics. *Joule* **4**, 1961–1976 (2020).
32. Miyazawa, Y. et al. Tolerance of perovskite solar cell to high-energy particle irradiations in space environment. *iScience* **2**, 148–155 (2018).
33. Tu, Y. et al. Mixed-cation perovskite solar cells in space. *Sci. China Phys. Mech. Astron.* **62**, 974221 (2019).
34. Xiao, X. et al. A unique Fe-N_4 coordination system enabling transformation of oxygen into superoxide for photocatalytic C-H activation with high efficiency and selectivity. *Adv. Mater.* **34**, 2200612 (2022).
35. Hayyan, M., Hashim, M. A. & AlNashef, I. M. Superoxide ion: generation and chemical implications. *Chem. Rev.* **116**, 3029–3085 (2016).
36. Wang, S. et al. Unveiling the role of tBP-LiTFSI. *complexes perovskite Sol. cells J. Am. Chem. Soc.* **140**, 16720–16730 (2018).
37. Guo, P. et al. Interfacial embedding of laser-manufactured fluorinated gold clusters enabling stable perovskite solar cells with efficiency over 24%. *Adv. Mater.* **33**, 2101590 (2021).
38. Guo, P. et al. Laser manufactured nano-MXenes with tailored halogen terminations enable interfacial ionic stabilization of high performance perovskite solar cells. *Adv. Energy Mater.* **12**, 2202395 (2022).
39. Chen, R. et al. Crown ether-assisted growth and scaling up of $FACsPbI_3$ films for efficient and stable perovskite solar modules. *Adv. Funct. Mater.* **31**, 2008760 (2021).

Acknowledgements

This work was financially supported by the project of the National Natural Science Foundation of China (52202115 (P.G.) and 52172101 (H.W.)), the Guangdong Basic and Applied Basic Research Foundation, China (2024A1515012325, P.G.), the National Key R&D Program for International Cooperation (2021YFE0115100, H.W.), the Natural Science Foundation of Chongqing, China (CSTB2022NSCQ-MSX1085, P.G.), the Shaanxi Science and Technology Innovation Team (2023-CX-TD-44, H.W.), the Shaanxi Province Key Research and Development Program (2022KWZ-04 and 2021ZDLGY14-08, H.W.), and by Spanish Ministry of Science and Innovation (PID2020-114796RB-C21/AEI/10.13039/501100011033, A.H.). Y. Zhou acknowledges the Excellent Young Scientists Fund (grant no. 52222318) from the National Natural Science Foundation of China and the startup grant support from HKUST. The authors would like to thank the Analytical

& Testing Center of Northwestern Polytechnical University and Shaanxi Materials Analysis and Research Center for XRD, XPS and SEM characterizations.

Author contributions

L.F.Y., J.W., and S.C.G. contributed equally to this work. P.G. and H.W. supervised the project. L.F.Y., J.W., and R.S. prepared and characterized the films and devices. S.C.G. conducted the stability tests. L.Y. and R.C. fabricated the PSC module. J.M.U., A.H., Z.L. and Y.Z. They helped analyze the experimental data. P.G. and L.F.Y. wrote the manuscript, and all the authors contributed to the general discussion.

Competing interests

The authors declare no competing interests.

Additional information

Supplementary information The online version contains supplementary material available at https://doi.org/10.1038/s41467-024-52199-4.

Correspondence and requests for materials should be addressed to Pengfei Guo or Hongqiang Wang.

Peer review information *Nature Communications* thanks Feng Wang and the other, anonymous, reviewer(s) for their contribution to the peer review of this work. A peer review file is available.